Extending the kinetic and thermodynamic limits of molecular-beam epitaxy utilizing suboxide sources or metal-oxide catalyzed epitaxy

Patrick Vogt,[1, *] Felix V. E. Hensling,[1] Kathy Azizie,[1] Jonathan P. McCandless,[2] Jisung Park,[1] Kursti DeLello,[3] David A. Muller,[3, 4] Huili G. Xing,[1, 2, 4] Debdeep Jena,[1, 2, 4] and Darrell G. Schlom[1, 4, 5, †]

[1]*Department of Materials Science and Engineering, Cornell University, Ithaca 14853, New York, USA*
[2]*School of Electrical and Computer Engineering, Cornell University, Ithaca 14853, New York, USA*
[3]*School of Applied and Engineering Physics, Cornell University, Ithaca 14853, New York, USA*
[4]*Kavli Institute at Cornell for Nanoscale Science, Ithaca 14853, New York, USA*
[5]*Leibniz-Institut für Kristallzüchtung, Max-Born-Str. 2, 12489 Berlin, Germany*

We observe a catalytic mechanism during the growth of III-O and IV-O materials by suboxide molecular-beam epitaxy (S-MBE). By supplying the molecular catalysts In_2O and SnO we increase the growth rates of Ga_2O_3 and In_2O_3. This catalytic action is explained by a metastable adlayer A, which increases the reaction probability of the reactants Ga_2O and In_2O with active atomic oxygen, leading to an increase of the growth rates of Ga_2O_3 and In_2O_3. We derive a model for the growth of binary III-O and IV-O materials by S-MBE and apply these findings to a generalized catalytic description for metal-oxide catalyzed epitaxy (MOCATAXY), applicable to elemental and molecular catalysts. We derive a mathematical description of S-MBE and MOCATAXY providing a computational framework to set growth parameters in previously inaccessible kinetic and thermodynamic growth regimes when using the aforementioned catalysis. Our results indicate MOCATAXY takes place with a suboxide catalyst rather than with an elemental catalyst. As a result of the growth regimes achieved, we demonstrate a Ga_2O_3/Al_2O_3 heterostructure with an unrivaled crystalline quality, paving the way to the preparation of oxide device structures with unprecedented perfection.

I. INTRODUCTION

Molecular-beam epitaxy (MBE) takes place under non-equilibrium conditions and surface kinetics plays a dominant role in the MBE growth process—allowing growth modes to be intentionally manipulated [1–5]. For decades, the single-step reaction mechanism occurring during the MBE growth of III-V (e.g., GaAs, GaN, AlN) [6–8] and II-VI (e.g., ZnSe, ZnO) [9, 10] compound semiconductors has defined MBE as a rather simple and straightforward thin film technique, especially when compared with chemical vapor deposition methods [11]. In contrast to the growth of III-V and II-VI materials, the surface kinetics of III-O (e.g., Ga_2O_3 and In_2O_3) [12–18] and IV-O (e.g., SnO_2) [19] compounds is governed by a complex reaction pathway, resulting in a two-step reaction mechanism to form the intended compound. The formation and subsequent desorption of ad-molecules, called suboxides (e.g., Ga_2O, In_2O, SnO), define the growth-limiting step for these classes of materials. The result is a rather narrow growth window within the adsorption-controlled regime [14, 15, 18–20].

By engineering the MBE processes, two variants of MBE have recently been developed. These variants extend the kinetic and thermodynamic limits within which III-O and IV-O materials may be grown. The first variant, *suboxide* MBE (S-MBE) [21], refers to a technique that uses the decomposition of III-VI and IV-VI compounds (i.e., Me_xO_y) by group III and IV elements [13, 17] as well as a special MBE source chemistry [21] to produce suboxide molecular beams that consist almost entirely (typically > 99.9%) of a single suboxide molecular species (i.e., Me_xO_{y-x}). Stoichiometric coefficients of Me_xO_y and Me_xO_{y-x} are $x = 2$ and $y = 3$ for III-O (e.g., Ga_2O_3, In_2O_3) and $x = 1$ and $y = 2$ for IV-O (e.g., SnO_2) materials.

Using the S-MBE approach, the growth-limiting step occurring during the growth of III-O and IV-O materials by conventional MBE is bypassed, enabling the growth of films with excellent structural quality and surface smoothness at growth rates exceeding $1 \, \mu m \, hr^{-1}$ and comparatively low growth temperature (T_G) [21]. The second variant is metal-oxide catalyzed epitaxy (MOCATAXY), a method involving the introduction of a catalyst into oxide growth systems [5, 17, 18, 22]. Using this technique, the growth-limiting step of III-O compounds is bypassed by the catalyst [5]. It has been proposed that MOCATAXY results from metal-exchange catalysis (MEXCAT) [5] and has been observed

on various growth surfaces for the formation of Ga_2O_3 and $(Al_xGa_{1-x})_2O_3$ [5, 18, 22–25] as well as during other physical vapor deposition methods [26]. Nevertheless, the underlying physics leading to the observed catalysis has been explained differently—experimentally [5, 22] and theoretically [27]—and thus remains disputable.

In this Letter, the combination of S-MBE and MO-CATAXY is investigated and shown to result in a marked extension of the kinetic and thermodynamic limits of the growth of Ga_2O_3 and In_2O_3. By supplying suboxide molecular beams of Ga_2O, In_2O, and SnO, a growth rate (Γ) enhancement of Ga_2O_3 and In_2O_3 is observed. Quantitative models describing this enhanced growth rate during S-MBE as well as during the catalyzed S-MBE of III-O thin films are derived and applied to the experimental observations to extract model parameters. Through a systematic comparison of experimental Γ data from different growth systems and growth methods (i.e., MOCATAXY during S-MBE and conventional MBE), a generalization of the proposed MEX-CAT mechanism [5] is developed. This generalized growth mechanism is applicable to the growth of Ga_2O_3 and In_2O_3 by conventional MBE and S-MBE.

II. SUBOXIDE MBE (S-MBE) MODEL

We begin by deriving a growth-rate model for the growth of III-VI and IV-VI compounds with general formula Me_xO_y by S-MBE and validate it by using Ga_2O_3 and In_2O_3 as examples. Figure 1 shows the growth kinetics of Ga_2O_3 and In_2O_3 as a function of their respective growth parameters. In panels (a)–(d), the film growth rate, Γ, is observed to increase linearly with the incident flux of suboxide, $\phi_{Me_xO_{y-x}}$ (i.e., ϕ_{Ga_2O} or ϕ_{In_2O}), in the O-rich regime. This linear increase in Γ reaches a plateau in the adsorption-controlled regime when $\phi_{Me_xO_{y-x}}$ exceeds the flux of active atomic oxygen, ϕ_o. The growth kinetics for the growth of III-O compounds by S-MBE are thus the same as those of III-V and II-VI materials when grown by conventional MBE [21].

Figures 1(e) and 1(f) depict Γ as a function of T_G and ϕ_o, respectively. For the same growth conditions, Γ of Ga_2O_3 on Ga_2O_3(010) [hollow squares] is larger than that of Ga_2O_3 on Ga_2O_3($\bar{2}$01) [solid squares]; see panel (e). This result is similar to the growth of Ga_2O_3 by conventional MBE on Ga_2O_3($\bar{2}$01) versus on Ga_2O_3(010) substrates [20, 28,
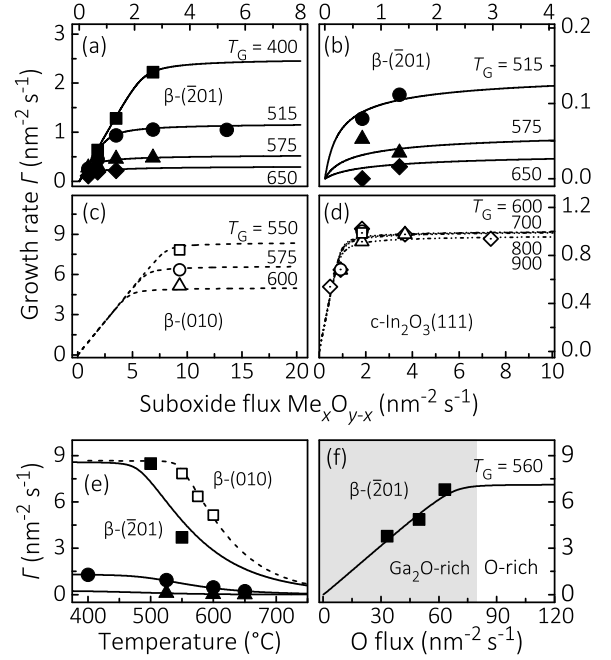

FIG. 1. (a) and (b) the dependence of the film growth rate (Γ, in units of the flux of Ga_2O being incorporated into the growing Ga_2O_3 film) of β-Ga_2O_3($\bar{2}$01) by S-MBE on the flux of the suboxide Ga_2O at active atomic oxygen fluxes $\phi_o = 5.7 \, nm^{-2} \, s^{-1}$ and $\phi_o = 0.7 \, nm^{-2} \, s^{-1}$, respectively. (c) Γ of β-Ga_2O_3(010) at $\phi_o = 33 \, nm^{-2} \, s^{-1}$ as a function of ϕ_{Ga_2O}. (d) Dependence of Γ of bixbyite In_2O_3(111) (in units of the flux of In_2O being incorporated into the growing In_2O_3 film) on the flux of the suboxide In_2O, at $\phi_o = 2.0 \, nm^{-2} \, s^{-1}$. (e) Growth temperature (T_G) dependence of Γ of β-Ga_2O_3($\bar{2}$01) and β-Ga_2O_3(010) at different active atomic oxygen fluxes: $\phi_o = 28.5 \, nm^{-2} \, s^{-1}$ (solid and hollow squares), $\phi_o = 5.7 \, nm^{-2} \, s^{-1}$ (solid circles), and $\phi_o = 0.7 \, nm^{-2} \, s^{-1}$ (solid triangles). The flux of Ga_2O supplied, ϕ_{Ga_2O}, corresponds to the vertical axis intercepts at low T_G. (f) Γ of β-Ga_2O_3($\bar{2}$01) as a function of ϕ_o at a constant value of ϕ_{Ga_2O} given by the vertical-axis intercept at high ϕ_o. Gray and white areas in (f) indicate the Ga_2O-rich and O-rich flux regimes, respectively. T_G in °C is indicated in the figures. Symbols are experimental data and lines are model predictions according to Eqs. (2)–(7) and the parameters given in Table I for the S-MBE growth of β-Ga_2O_3($\bar{2}$01) [solid symbols and lines], β-Ga_2O_3(010) [hollow symbols and dashed lines], and bixbyite In_2O_3(111) [hollow symbols with a dot in their center and dashed-dotted lines]. Data in (a) are taken from Ref. [21]

.

29]. Comparing the growth kinetics of Ga_2O_3($\bar{2}$01) and In_2O_3(111) [e.g., the data in panel (a) with the data in panel (d)] establishes that the range of T_G within which high-quality films of In_2O_3 can be grown at high Γ is larger than that for

Ga_2O_3. This result is also similar to the growth of Ga_2O_3 and In_2O_3 by conventional MBE [13, 15, 18].

To model the growth of binary oxides (Me_xO_y) from their suboxides (Me_xO_{y-x}), we take the single-step reaction kinetics of S-MBE [21] into account. Here, the growth takes place via the reaction

$$Me_xO_{y-x}(a) + xO(a) \xrightarrow{\kappa} Me_xO_y(s), \qquad (1)$$
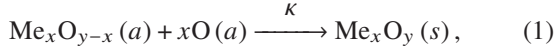
with constant κ describing the Me_xO_y formation rate. Adsorbate and solid phases are denoted as a and s, respectively. Based on reaction (1), we set up a generalized growth-rate model describing the growth of these materials by S-MBE:

$$\frac{dn_r}{dt} = \phi_r - \kappa n_r n_o^x - \tau_r^{-1} n_r, \qquad (2)$$

$$\frac{dn_o}{dt} = \varsigma \phi_o - x\kappa n_r n_o^x - \tau_o^{-1} n_o, \qquad (3)$$

$$\frac{dn_p}{dt} = \Gamma = \kappa n_r n_o^x. \qquad (4)$$

The surface densities of adsorbed cationic reactants ($r = Me_xO_{y-x}$), O adsorbates, and formed products ($p = Me_xO_y$) are denoted as n_r, n_o, and n_p, respectively. Their time derivative is described by the operator d/dt. The surface lifetimes of r and O are given by τ_r and τ_o, respectively. The T_G-, orientation-, and growth-system-dependent sticking probability ς of O can be derived by considering two competing processes: the chemisorption of O and the desorption of O from the given adsorption sites, described by the reaction rates k_c and k_d, respectively,

$$k_i = \nu_i e^{-\frac{\varepsilon_i}{k_B T_G}}, \qquad (5)$$

with $i = c, d$, frequency factor ν_i, and the respective energy barrier ε_i. Following the Kisliuk model [30], the O sticking probability $0 \leq \varsigma \leq 1$ [31, 32] is given by

$$\varsigma = \frac{k_c}{k_c + k_d} = \left(1 + \nu e^{-\frac{\delta\varepsilon}{k_B T_G}}\right)^{-1} \qquad (6)$$

with dimensionless pre-factor $\nu = \nu_d/\nu_c$ and activation barrier $\delta\varepsilon = \varepsilon_d - \varepsilon_c$. In the case of a high O desorption barrier or a high O adsorption barrier, the limits of Eq. (6) are (i) $\varepsilon_d \gg \varepsilon_c \Rightarrow \delta\varepsilon \gg 0 \Rightarrow \varsigma \to 1$ and (ii) $\varepsilon_c \gg \varepsilon_d \Rightarrow \delta\varepsilon \ll 0 \Rightarrow \varsigma \to 0$, respectively, satisfying our conditions of $0 \leq \varsigma \leq 1$. Figure 2 depicts the model results of Eq. (6) of our model for Ga_2O_3 and In_2O_3 using the parameters given in Table I.

	ν	$\delta\varepsilon$ (eV)	P_0 (nm^{2x})	$\mathcal{E}$ (eV)
β-$Ga_2O_3(\bar{2}01)$	$e^{16.1\pm1}$	1.07 ± 0.1	$e^{0.15\pm0.05}$	0.12 ± 0.01
β-$Ga_2O_3(010)$	$e^{16.6\pm1}$	1.20 ± 0.2	$e^{0.25\pm0.09}$	0.15 ± 0.03
$In_2O_3(111)$	$e^{28.4\pm1}$	3.21 ± 0.5	$e^{0.90\pm0.10}$	0.25 ± 0.02

TABLE I. Parameters ν, $\delta\varepsilon$, P_0, and $\mathcal{E}$ obtained using an iterative approach of the growth model to the flux-dependence of the growth rate (Γ) of $Ga_2O_3(\bar{2}01)$, $Ga_2O_3(010)$, and $In_2O_3(111)$ by S-MBE with Eqs. (2)–(7).

Solving Eqs. (2) and (3) with respect to n_r and n_o and inserting their solutions into Eq. (4) yields an analytical expression for Γ described by three kinetic parameters: κ, τ_r, and τ_o, see Eqs. (17)–(23). To reduce the complexity of the model we assume that O adsorbate desorption is negligible and use $\kappa \gg \tau_r^{-1}$ and $\tau_r \ll \tau_o$. Assuming that the observed reaction processes follow a thermally activated Arrhenius behavior, we further reduce the complexity of our model by forming the product

$$P(T_G) = \tau_r \kappa = P_0 e^{\left(\frac{\mathcal{E}}{k_B T_G}\right)}, \qquad (7)$$

with pre-exponential factor $P_0 = \tau_r^0 \kappa_0$ and activation energy $\mathcal{E} = \varepsilon_{\tau_r} - \varepsilon_\kappa$. The latter expression yields a larger κ or a longer τ_r the higher the growth rate Γ of the intended compound. This is in agreement with experiment as shown in Fig. 1.

We apply the solution of this model to the binary growth rate data of Ga_2O_3 and In_2O_3 by S-MBE depicted in Fig. 1 and extract the kinetic parameters summarized in Table I. To extract the parameters we use an iterative approach. For ex-
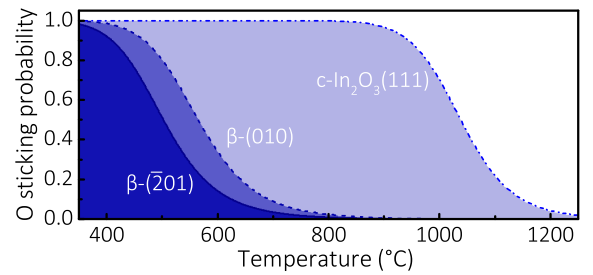

FIG. 2. Oxygen sticking probability ς as a function of the growth temperature T_G. Solid, dashed, and dashed-dotted lines represent ς of β-$Ga_2O_3(\bar{2}01)$ (the dark blue area), β-$Ga_2O_3(010)$ (the blue area), and bixbyite (cubic) c-$In_2O_3(111)$ (the pale blue area), respectively. The lines are modeled by Eq. (6) using the parameters given in Table I for the respective phases.

ample, for the growth of Ga_2O_3 by S-MBE we first establish that the functional form of the equations accurately describe the growth of $(\bar{2}01)$ oriented β-Ga_2O_3 films, as plotted in Figs. 1(a) and 1(b). Having established that the functional form of the equations [solutions given by Eqs. (17)–(23)] accurately describe the growth of $(\bar{2}01)$ oriented β-Ga_2O_3 films, the model is next expanded to an additional orientation, (010) β-Ga_2O_3 films using the data in Fig. 1(c).

Orientation-dependent growth rate of β-Ga_2O_3

As a quantitative result, we find that the range of T_G that can be used to produce high-quality epitaxial films at high Γ (i.e., a growth window) of $(\bar{2}01)$-oriented Ga_2O_3 films is narrower than for the growth of (010)-oriented Ga_2O_3 films, which, in turn, is narrower than the one for the growth of (111)-oriented In_2O_3 films. This is because of the different reaction efficiencies, η, of Ga_2O and In_2O with active O species (more detailed explanation below in the text). In addition, we explain the different sticking probabilities ς, e.g., as obtained for $Ga_2O_3(\bar{2}01)$ and $Ga_2O_3(010)$, by the activity of surface reactions between Ga_2O and O adsorbates being dependent on the orientation of the surface on which the reaction takes place. In other words, the reservoir of active atomic oxygen for Ga_2O oxidation on $Ga_2O_3(010)$ is larger than the one on $Ga_2O_3(\bar{2}01)$. This finding can be transferred to the growth of Ga_2O_3 by conventional MBE where a similar dependence of Ga_2O_3 growth rate is observed. We propose that this Γ dependence results from an orientation-dependent activity of the oxidation of Ga_2O to Ga_2O_3 [14, 20] and that the underlying reason is due to the orientation-dependent vertical and lateral bond strengths between ad-atoms and the substrate surfaces [28, 29]. In Refs. [20, 28, 29] the orientation dependence of the growth rate on the (hkl) plane, $\Gamma_{(hkl)}$, is given for β-Ga_2O_3: $\Gamma_{(010)} > \Gamma_{(001)} > \Gamma_{(\bar{2}01)} > \Gamma_{(100)}$. We observe this same order of growth rate as a function of surface orientation for the growth of Ga_2O_3 by S-MBE, and conclude that the orientation-dependent values of the sticking probability $\varsigma_{(010)} > \varsigma_{(001)} > \varsigma_{(\bar{2}01)} > \varsigma_{(100)}$ can be related to the orientation-dependent reaction activities of adorbates, underlying the observed order of $\Gamma_{(hkl)}$ for β-Ga_2O_3, see Fig. 2.

III. MOCATAXY COMBINED WITH S-MBE

We next describe the enhancement to the growth rate of Ga_2O_3 and In_2O_3 due to the presence of the catalysts In_2O and SnO, i.e., the combined effects of S-MBE and MOCATAXY. As depicted in Figs. 3(a)–3(c), we observe a drastic enhancement in Γ of heteroepitaxial β-$Ga_2O_3(\bar{2}01)$ grown on $Al_2O_3(0001)$ and homoepitaxial β-$Ga_2O_3(010)$ grown on β-$Ga_2O_3(010)$ using the suboxides In_2O and SnO as catalysts. The catalytic effect of SnO on the growth rate of Ga_2O_3 is stronger than that of In_2O. It is also stronger for the growth of β-$Ga_2O_3(\bar{2}01)$ (solid symbols) than for the growth of β-$Ga_2O_3(010)$ (hollow symbols). The stronger catalytic effect of SnO compared with In_2O can be explained by their different vapor pressures, i.e., $P_{SnO} < P_{In_2O}$ [34–36]. Thus, under similar growth conditions, the surface lifetime of SnO is longer than that of In_2O. Hence, SnO can be re-oxidized more often than In_2O [5, 17], and the O reservoir that ultimately ends up oxidizing Ga_2O in the presence of SnO is larger than that for Ga_2O oxidation in the presence of In_2O. Figures 3(d)–3(f) depict Γ of Ga_2O_3 as a function of ϕ_{In_2O} and ϕ_{SnO}, respectively. When SnO is used as a catalyst it is evident from the data that the catalytic effect on $Ga_2O_3(\bar{2}01)$ is stronger than it is on $Ga_2O_3(010)$. As shown below in Eq. (16), the catalytic activity, α, decreases with increasing O flux. Therefore, the weaker catalytic effect observed on β-$Ga_2O_3(010)$ compared with the effect on β-$Ga_2O_3(\bar{2}01)$ may be explained by the higher surface-dependent sticking probability $\varsigma_{(010)} > \varsigma_{(\bar{2}01)}$ (values are given in Table I). Further studies on the atomic incorporation and surface segregation of residual Sn and In in the grown thin films, when using SnO and In_2O as catalysts, respectively, need to be performed. Nevertheless, energy-dispersive x-ray spectroscopy (EDXS), secondary-ion mass spectrometry (SIMS), and atomic probe tomography (APT) have already shown that the concentrations of In [5, 18, 24] and Sn [22] in Ga_2O_3 as well as in $(Al_xGa_{1-x})_2O_3$ films are below 1 %. This is consistent with our x-ray diffraction (XRD) results showing only diffraction peaks from Ga_2O_3 in the thin films, an example of which is shown in Fig. 4.

Comparing Figs. 3(f) and 3(g) reveals that the growth rates Γ of β-$Ga_2O_3(\bar{2}01)$ and β-$Ga_2O_3(010)$ using solely SnO and SnO + In_2O as catalysts are very similar (under otherwise identical growth conditions). We thus conclude that SnO

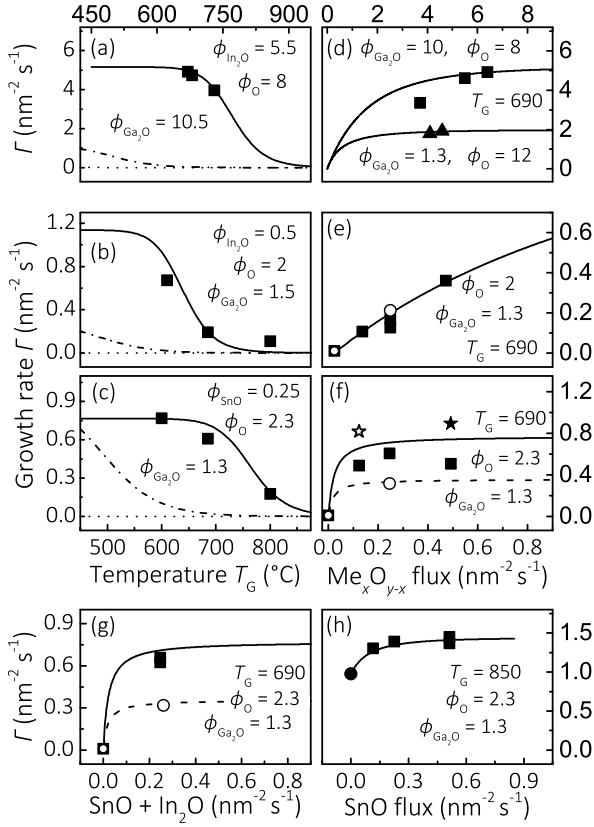FIG. 3. (a)–(c) Γ of β-Ga$_2$O$_3$($\bar{2}$01) as a function of T_G in the presence of either the catalyst In$_2$O or SnO at the steady state fluxes given. (d)–(g) Γ of β-Ga$_2$O$_3$($\bar{2}$01) (solid symbols) and β-Ga$_2$O$_3$(010) (hollow symbols) as a function of the In$_2$O flux as a catalyst [panels (d) and (e)], SnO flux as a catalyst [panel (f)], and their sum a In$_2$O + $(1-a)$ SnO as competing catalysts (with $a = 0.5$) [panel (g)]. (h) Γ of bixbyite In$_2$O$_3$(111) using SnO as a catalyst. Solid lines are model predictions by the catalytic model, Eqs. (10)–(16). The parameters used for our model predictions are given in Table II. Dashed-dotted and dotted lines depict the model predictions for the growth of β-Ga$_2$O$_3$ by S-MBE [Eqs. (2)–(7)] and conventional MBE [33] in the absence of a catalyst, respectively. The units of the fluxes given in the figures are nm^{-2} s^{-1}; the temperature T_G are in °C. The values of ϕ_O correspond to the maximum available active atomic oxygen provided by the catalyst (i.e., In$_2$O or SnO). Additional characterizations of the sample grown at the conditions depicted by the solid star in (f) are provided in Fig. 4.

suppresses In$_2$O as a catalyst, i.e., the catalytic effects are not additive: the presence of SnO inhibits (or isolates) the catalytic activity of In$_2$O in the SnO–In$_2$O–Ga$_2$O–O system. We predict the same effect for MOCATAXY by conventional MBE, i.e., when using the elemental catalysts In [5] and Sn [22] in combination for the growth of Ga$_2$O$_3$ in the Sn–In–

Ga-O system.

Figure 3(h) shows the catalytic effect of SnO on Γ of In$_2$O$_3$(111) grown on Al$_2$O$_3$(0001) substrates. The solid circle in Fig. 3(h) corresponds to the growth rate of In$_2$O$_3$ determined by x-ray reflectivity (XRR) in the absence of SnO. In the presence of SnO, the growth rate of In$_2$O$_3$ (again measured by XRR) is seen to increase by a factor of ∼ 1.4, i.e., far larger than the effect caused by additional SnO incorporation into In$_2$O$_3$. SIMS [37] and x-ray fluorescence (XRF) [37] were used to quantify the Sn content present in the In$_2$O$_3$ films grown with the SnO catalyst. A value of ≈ 3 % Sn in In$_2$O$_3$ was observed by SIMS and XRF independent of the SnO fluxes in the $(0.2 - 0.5)$ nm^{-2} s^{-1} range.

This result indicates that SnO increases the available O reservoir for the oxidation of In$_2$O to In$_2$O$_3$ by a factor of ∼ 1.4 (at these growth conditions). This finding is in line with the data plotted in Figs. 3(f) and 3(g), i.e., that SnO has a higher reactivity with O than In$_2$O. We explain the catalytic action of SnO on In$_2$O by their different vapor pressures $P_{SnO} < P_{In_2O}$ [34–36]. Thus, SnO provides a larger O reservoir for In$_2$O oxidation than is available in the absence of SnO. The In$_2$O-SnO-O system is the first catalytic system observed for MBE growth beyond Ga$_2$O$_3$-based systems [5, 18, 22–25]. The discovery of MOCATAXY during S-MBE and its extension to In$_2$O$_3$ suggests its universality for the MBE growth of a multitude of oxide compounds (during S-MBE as well as conventional MBE).

We explain the observed catalysis during the growth of Ga$_2$O$_3$ and In$_2$O$_3$ by S-MBE by the formation of a metastable adlayer A between the catalyst c and O, e.g., $A =$ In$_2$O–O or $A =$ SnO–O. As experimentally and mathematically shown by Fig. 1, Table I, and Eqs. (2)–(6), In$_2$O possesses a higher surface reactivity with active O than does Ga$_2$O, leading to a higher growth rate of In$_2$O$_3$ compared with Ga$_2$O$_3$ at comparable growth conditions. This behavior is similar to the growth of Ga$_2$O$_3$ and In$_2$O$_3$ by conventional MBE [13, 16], which was explained by the different oxidation efficiencies η of the elements Sn, In, and Ga following the order: $\eta_{Sn} \approx 1.1\,\eta_{In} \approx 3.1\,\eta_{Ga}$ [5, 13, 17]. Taking the ratio of maximum available O for Ga$_2$O and In$_2$O oxidation (data plotted in Figs. 1(b) and 1(d) and flux conversions given in Eqs. (27) from mixtures of O$_2$ and 10% O$_3$ [38] at a background pressure of 1×10^{-6} Torr, we obtain $\eta_{In_2O} \approx 2.8\,\eta_{Ga_2O}$. This result is very similar to $\eta_{In} \approx 2.8\,\eta_{Ga}$ [5, 13, 17] ob-

served during conventional MBE growth. We surmise following Ref. [17] that the same value of η observed during MOCATAXY in conventional MBE and S-MBE arises from what is the second reaction step of conventional MBE and the sole reaction step of S-MBE, where the suboxide reacts with O to complete the formation of the intended oxide (e.g., $Ga_2O \rightarrow Ga_2O_3$) [18] and *not* to the suboxide formation step (e.g., $Ga \rightarrow Ga_2O$) [18]. Thus, for the discussion and analysis that follow we use $\eta_{SnO} \approx 1.1\,\eta_{In_2O} \approx 3.1\,\eta_{Ga_2O}$ during S-MBE. These oxidation efficiencies follow the same order in η as was observed for growth by conventional MBE [5, 17].

A. Generalized metal-exchange catalytic model

We propose that the role of the catalyst c (e.g., In_2O, SnO, In [5], or Sn [22]) is to increase the O adsorbate reservoir of the reactant r (e.g., Ga_2O or Ga) by forming A through the reaction

$$c\,(a) + O\,(a) \rightarrow A\,(a)\,, \qquad (8)$$
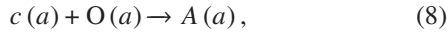
with examples of A being In_2O–O, In–O, SnO–O, or Sn–O. In the presence of r, A is unstable and catalyzes the incorporation of r into the intended product p (e.g, Ga_2O_3), while decreasing the reaction barrier of r with O. Thus, reaction (8) is subsequently followed by the reaction

$$Me_xO_{y-x}\,(a) + xA\,(a) \rightarrow Me_xO_y\,(s) + c\,(a)\,. \qquad (9)$$
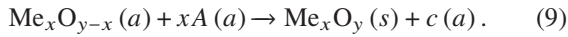
Equation (9) describes the consumption of A while forming the product $p = Me_xO_y$) and releasing c on the growth surface. The catalyst c may be re-oxidized [5], leading to an increase in the available O reservoir for the reactant ($r = Me_xO_{y-x}$), and thus to an extension of the kinetic and thermodynamic limits to the formation of p.

An adlayer formed by In has also been observed during the formation of GaN using In as a surface active agent (surfactant) [3]. Here, the In adlayer enables an enhanced diffusion channel for the Ga and N adsorbates. Moreover, a surface instability of In–O bonds in the presence of Fe [39] and Ga [5] has been observed during conventional MBE. We emphasize, however, the catalytic effect we are describing must not be confused with effects resulting from surfactants during the growth of III-V compounds by conventional MBE [2–4].

In order to describe MOCATAXY for elemental (e.g., In [5] and Sn [22]) and molecular catalysts (e.g., In_2O and SnO) as well as for different materials (e.g., Ga_2O_3 and In_2O_3) mathematically, we would have to take into account the surface populations of c, r, and atomic O together with the surface density of the p that forms following the Langmuir-Hinshelwood mechanism [40]. We may reduce the complexity of the model significantly by only taking into account the most likely reactions involved in the formation of p, following the Eley-Rideal formalism [41]. The resulting set of coupled differential equations reads:

$$\frac{dn_c}{dt} = \phi_c - \sigma n_c(1 - \theta_A)\phi_o + \alpha\phi_r\theta_A^x - \gamma_c n_c\,, \qquad (10)$$

$$\frac{d\theta_A}{dt} = \sigma n_c(1 - \theta_A)\phi_o - \alpha\phi_r\theta_A^x\,, \qquad (11)$$

$$\frac{dn_P}{dt} \equiv \Gamma = \alpha\phi_r\theta_A^x\,, \qquad (12)$$

with the adatom density n_c and desorption rate constant γ_c of the catalyst c, as well as the surface coverage θ_A of A. The second and third terms in Eq. (10) refer to the formation rates of A and p, respectively, and the factor $(1 - \theta_A)$ assures that A constitutes a surface phase. The last term in Eq. (10) accounts for the desorption of c from the growth surface, and σ (with the dimension of nm^2) represents the cross section of colliding c with O [5]. The impinging fluxes of c and r are denoted as ϕ_c and ϕ_r, respectively. We note that the structure of the model introduced here is similar to the MEXCAT model given in Ref. [5]. The improvement of the model given in this work and its generalization to elemental and molecular catalysts arises by taking a cationic-like, metastable adlayer A into account. This allows MOCATAXY to be described for the growth of ternary systems involving molecular catalysts [e. g., In_2O (Fig. 3) and SnO (Fig. 3)] as well as elemental catalysts [e. g., In (Fig. 5) and Sn (Fig. 5)].

B. Suboxide catalysts

Our results thus indicate that MOCATAXY takes place with a suboxide catalyst (e.g., for A being In_2O–O or SnO–O) and *not* with an elemental catalyst (e.g., for A being In–O or Sn–O). For conventional MBE, i.e., when using elemental source materials, we assume the reaction of the metal to form the suboxide (e.g., $2Ga + O \rightarrow Ga_2O = r$) occurs very rapidly [33], and thus, the catalysis takes place between the suboxide reactant r and A, satisfying reactions (8) and (9). Should the

reaction of 2Ga+O → Ga$_2$O not occur very rapidly, we would see Ga desorption (at least a fraction of it), and a plateau in Γ in the adsorption-controlled regime during the growth of Ga$_2$O$_3$ by conventional MBE; similar to the Γ plateau, e.g., observed during the growth of GaN by conventional MBE [8]. The subsequent desorption of the rapidly formed Ga$_2$O is the growth-rate-limiting step in conventional MBE as it removes active O from the growth front (by forming Ga$_2$O), leading to the decrease in Γ in the adsorption-controlled regime as well as at elevated T_G [12, 17, 33]. In S-MBE, the formation of Ga$_2$O (through 2Ga + O → Ga$_2$O) is bypassed since Ga$_2$O is directly provided from the source. Therefore, the O-consuming step is now avoided and a plateau in Γ of Ga$_2$O$_3$ in the adsorption-controlled regime occurs [21]. The assumption that MOCATAXY takes place with a suboxide catalyst is further supported by our finding in this work that the oxidation efficiency η for In$_2$O and Ga$_2$O during MOCATAXY by S-MBE follows the same order in η as for Ga and In during conventional MBE, i.e., $\eta_{In_2O} = 2.8\eta_{Ga_2O}$ for S-MBE [this work] versus $\eta_{In} = 2.8\eta_{Ga}$ for conventional MBE [5, 17]. Nevertheless, we emphasize that the microscopic origin and reaction pathways of MOCATAXY during S-MBE and conventional MBE requires further investigation to fully understand which species are indeed involved leading to the observed catalysis given in this work and presented in Refs. [5, 17, 18, 22–27].

Solving Eqs. (10) and (11) with respect to n_c and θ_A yields $\phi_c = \gamma_c n_c$, consistent with our observation of negligible incorporation ($\approx 3\,\%$) of c into the grown thin films for the data plotted in Fig. 3. Inserting the solution for θ_A into Eq. (12) yields the following expression, valid for first-order kinetics with $x = 1$,

$$\Gamma = \frac{\alpha \phi_c \phi_r \phi_o}{\alpha J \phi_r + \phi_c \phi_o} \ . \tag{13}$$

The free parameters are the pseudo-flux

$$J = \frac{\gamma_c}{\sigma} = J_0 \exp\left(-\frac{\Delta}{k_B T_G}\right) \tag{14}$$

with $J_0 = 1 \times 10^{14}\,\mathrm{nm^{-2}\,s^{-1}}$ (assumed for all species as a first approximation [31]) and energy Δ. The value of Δ depends linearly on ϕ_c (e.g., ϕ_{In_2O} and ϕ_{SnO}),

$$\Delta(\phi_c) = \Delta_0 + \delta \phi_c\,, \tag{15}$$

with Δ_0 denoting the evaporation enthalpy, e.g, of In$_2$O and SnO, and δ describing its increase with increasing ϕ_c. The

	Δ_0 (eV)	δ (meV nm^2 s)	b (nm^2 s)
β-Ga$_2$O$_3$($\bar{2}$01):In$_2$O	2.6 ± 0.05 [35]	30 ± 2	0.07 ± 0.01
β-Ga$_2$O$_3$(010):In$_2$O	2.6 ± 0.05 [35]	30 ± 2	0.07 ± 0.01
β-Ga$_2$O$_3$($\bar{2}$01):SnO	2.9 ± 0.05 [34]	50 ± 4	0.20 ± 0.03
β-Ga$_2$O$_3$(010):SnO	2.9 ± 0.05 [34]	10 ± 1	0.33 ± 0.05
In$_2$O$_3$(111):SnO	3.2 ± 0.05	400 ± 10	0.33 ± 0.05

TABLE II. The values of Δ_0, δ, and b used in Eqs. (15) and (16) for different catalytic systems and growth surfaces.

other free parameter is the catalytic activity coefficient, α. For α (ranging from 1 to 0), we use a linear approximation depending on impinging ϕ_o, i.e.,

$$\alpha(\phi_o) = 1 - b\phi_o\,, \tag{16}$$

with b describing the decrease of α with ϕ_o. By an iterative approach of our model to the experimental growth rate data, the values obtained of Δ_0, δ, and b for In$_2$O and SnO are given in Table II.

The evaporation enthalpies Δ_0 of In$_2$O and SnO on Ga$_2$O$_3$ surfaces correspond to the values given in the literature, as noted in Table II. Only the value of Δ_0 for SnO on the In$_2$O$_3$(111) surface is slightly above the literature value, indicating an additional energy term caused by vertical and lateral interactions between adsorbed species and the In$_2$O$_3$(111) surface. The increase in Δ with ϕ_c, described by the parameter δ, indicates an increase in lateral adsorbate binding energy with increasing $\phi_c \propto n_c$. An analogous behavior has also been observed for the desorption kinetics of In on Ga$_2$O$_3$ [5] and Ga on GaN [42]. We explain the linear decrease of α with ϕ_o by a linear increase of O adsorbates with ϕ_o, i.e., $\phi_o \propto n_o$. It has been shown that an increase in ϕ_o promotes the incorporation of In during the growth of (In$_x$Ga$_{1-x}$)$_2$O$_3$ by conventional MBE; this decreases the catalytic strength of In for the formation of Ga$_2$O$_3$ [5, 16, 17, 29]. We therefore explain the decrease in α with increasing $\phi_o \propto n_o$ by a decreasing diffusion length of c and r, and thus, a decrease in the probability of reaction (9) to occur.

C. Elemental catalysts

We have applied the above model to the data published in Refs. [5] and [22] for MOCATAXY during conventional MBE growth of Ga$_2$O$_3$, i.e., using elemental In and Sn as

catalysts (see Appendix). For the former, our model and the parameters given in this Letter can describe the data published in Ref. [5] with the same accuracy. For the latter, we provide the first mathematical description of a catalytic system involving the element Sn (see Appendix). These results, and the comparison among different MBE variants (i.e., S-MBE and conventional MBE), confirm the accuracy of our refined and generalized MEXCAT model, describing MOCATAXY for elemental and molecular catalysts.

D. Obtained 'pseudo' Ga$_2$O$_3$/Al$_2$O$_3$ heterostructure

As a result of combining S-MBE with MOCATAXY, in Figs. 4(a)–4(d), we demonstrate an unprecedented 'pseudo' β-Ga$_2$O$_3$($\bar{2}$01)/Al$_2$O$_3$(0001) heterostructure with unparalleled crystalline perfection. Figure 4(a) shows θ-2θ x-ray diffraction (XRD) scans of a 90 nm thick SnO-catalyzed Ga$_2$O$_3$ film (black trace) and a 40 nm thick non-catalyzed Ga$_2$O$_3$ film grown by S-MBE under similar growth conditions (T_G = 500 °C, ϕ_{Ga_2O} = 0.9 nm^{-2} s^{-1}, and ϕ_o = 2.3 nm^{-2} s^{-1}). The SnO-catalyzed Ga$_2$O$_3$ film is the same film that is plotted in Fig. 3(f) as a solid-black star. It was grown at T_G = 690 °C, ϕ_{Ga_2O} = 1.3 nm^{-2} s^{-1}, and ϕ_o = 2.3 nm^{-2} s^{-1}. The reflections of the non-catalyzed Ga$_2$O$_3$ thin film coincide with the β-Ga$_2$O$_3$($\bar{2}$01) phase grown with its ($\bar{2}$01) plane parallel to the (0001) plane of the Al$_2$O$_3$ substrate. In contrast, the XRD scan of the SnO-catalyzed Ga$_2$O$_3$ film shows only the even reflections of the β-Ga$_2$O$_3$ phase grown with its ($\bar{2}$01) plane parallel to the (0001) plane of the Al$_2$O$_3$ substrate. We speculate that the 'pseudo' β-Ga$_2$O$_3$($\bar{2}$01)/Al$_2$O$_3$(0001) contains an aperiodic occurrence of low-energy stacking faults, parallel to the ($\bar{2}$01) plane of the Ga$_2$O$_3$ film that reduce the number of the observed XRD diffraction peaks of the 'pseudo' β-Ga$_2$O$_3$($\bar{2}$01) phase. This hypothesis is consistent with calculations showing that the stacking fault energy in β-Ga$_2$O$_3$ is low [43, 44], experimental observation of high densities of stacking faults in β-Ga$_2$O$_3$ films [45], and the scanning transmission electron microscopy (STEM) image depicted in Fig. 4(b). The epilayer shows a single-crystalline structure with an abrupt interface to the Al$_2$O$_3$(0001) substrate at the bottom of the image. Figure 4(c) shows a transverse scan (rocking curve) across the symmetric $\bar{4}$02 reflection of the same 'pseudo' β-Ga$_2$O$_3$($\bar{2}$01) film. The measured full width at half max-
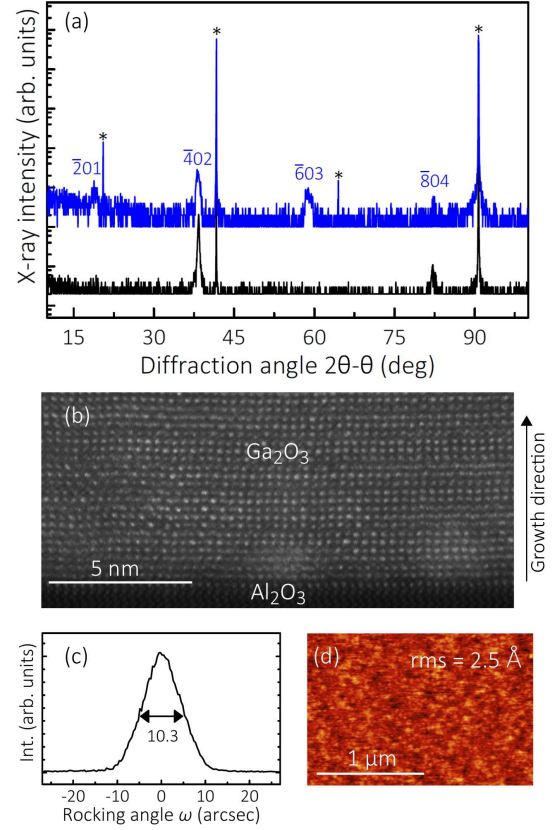

FIG. 4. (a) Longitudinal XRD scans recorded from an SnO-catalyzed Ga$_2$O$_3$ film (black trace) and a non-catalyzed β-Ga$_2$O$_3$($\bar{2}$01) film (blue trace) grown by S-MBE on Al$_2$O$_3$(0001) substrates. Reflections labeled by an asterisk originate from the substrate. The reflections from the Ga$_2$O$_3$ films are marked in the figure. (b) STEM image along the [100] zone axis of the Ga$_2$O$_3$ thin film. (c) Transverse XRD scan across the $\bar{4}$02 peak of the same SnO-catalyzed Ga$_2$O$_3$ film [black trace in (a)], with its full width at half maximum indicated in the figure. (d) Surface morphology of the same film SnO-catalyzed Ga$_2$O$_3$ film; it has a root means square roughness of 2.5 Å. The data depicted in (a) [black trace], (b), (c), and (d) were taken from the same Ga$_2$O$_3$ film plotted by the solid star in Fig. 3(f).

imum (FWHM) is just $\Delta\omega \approx 10$ arcsec; this is a measure of the out-of-plane mosaic spread of the thin film. Figure 4(d) depicts an atomic force microscope (AFM) image of the surface morphology of the same SnO-catalyzed Ga$_2$O$_3$ film; it has a root mean square roughness (rms) of 2.5 Å. The obtained rocking curve of $\Delta\omega \approx 10$ arcsec and smooth surface morphology of rms = 2.5 Å provide the best results obtained for any Ga$_2$O$_3$ thin film grown on Al$_2$O$_3$(0001) by any method. We point out that optimizations utilizing the unprecedented growth regimes—becoming accessible by the

combination of *S*-MBE with MOCATAXY—still need to be performed to further improve the crystalline perfection of the grown Ga$_2$O$_3$-based heterostructures.

We note that in the absence of a catalyst, Ga$_2$O$_3$ does not form at this high T_G of 690 °C. In addition, at a lower catalyst flux of SnO [depicted as the open star in Fig. 3 (f)] compared with the sample grown at a higher SnO flux [depicted as the solid star in Fig. 3 (f) and Fig. 4] we have not measured the 'pseudo' β-Ga$_2$O$_3$($\bar{2}$01) phase, but instead see the 'conventional' β-Ga$_2$O$_3$($\bar{2}$01) peaks by XRD (data not shown in this work). We therefore conclude that extending the kinetic (e.g., higher possible T_G) and thermodynamic limits (e.g., different surface chemical potential) by combining *S*-MBE with MOCATAXY benefits the formation of the 'pseudo' β-Ga$_2$O$_3$($\bar{2}$01)/Al$_2$O$_3$(0001) heterostructure that has unparalleled crystalline perfection.

IV. CONCLUSION

As we have demonstrated, the nature of the model derived to describe MOCATAXY using elemental and molecular catalysts does *not* depend on the specific growth surface. We note, however, that the growth surface may change the kinetic parameters used in our model as shown for the examples of β-Ga$_2$O$_3$($\bar{2}$01) and β-Ga$_2$O$_3$(010) using In$_2$O or SnO as catalysts in this work.

Finally, the increase in the growth rates of Ga$_2$O$_3$ and In$_2$O$_3$ by *S*-MBE that occur when using the catalysts SnO and In$_2$O, demonstrates MOCATAXY as a potentially inherent feature in conventional MBE growth [5, 18, 22–25] as well as in *S*-MBE growth. Furthermore, our results provide deeper insight into this catalysis, indicating MOCATAXY occurs through a suboxide catalyst rather than with an elemental catalyst. This more broad applicability of MOCATAXY opens an unprecedented path for the epitaxial synthesis of thin films by intentionally extending the kinetic and thermodynamic limits during their growth processes. If successful, this could enable the growth of (yet) unknown crystal phases and unprecedented functional electronic materials.

V. APPENDIX

We apply the generalized MOCATAXY model, Eqs. (10)–(16), to published catalytic data using elemental In [5] and elemental Sn [22] as catalysts for the growth of Ga$_2$O$_3$ by MBE. The parameters used in Eqs. (15) for In and Sn are collected in Table III. Within experimental uncertainty, the obtained Δ_0 corresponds to the vaporization enthalpies of elemental In [46] and Sn [34] as given in the literature; the values are given in Table III. Moreover, for our model we use $\alpha = 1$ (the catalytic activity), the same value of α as used in Ref. [5].

Figures 5(a) and 5(b) show our results for the growth of Ga$_2$O$_3$ by MBE when supplying In and Sn as elemental catalysts, respectively. Our model drawn in Fig. 5(a) (solid lines) describes the data published in Ref. [5] with the same accuracy as the previously established metal-exchange catalysis (MEXCAT) model [5]. Figure 5(b) plots the catalyzed growth rate data of Ga$_2$O$_3$ taken from Ref. [22]. Our model applied to this data is drawn as the solid line. It precisely describes the Sn-catalyzed growth of Ga$_2$O$_3$ by MBE and is the first quantitative description of MOCATAXY using Sn as a catalyst. To model the Sn-catalyzed data, we linearly extrapolated the value of ϕ_O^{Sn} given in Eq. (29) while using the O flux conditions published in Ref. [22].

To conclude, our model introduced in the main text is able to the describe the growth of Ga$_2$O$_3$ and In$_2$O$_3$ by *S*-MBE as well as conventional MBE when using elemental and molecular catalysts. This is achieved by introducing a cationic-like, catalytic adlayer A.

A. Detailed model of the growth of III-VI materials by *S*-MBE

The analytical solution of the growth rate, Γ, of Eqs. (2)–(4) for III-VI compound materials is:

$$\Gamma = \left(\zeta_-^2 P^2 + \xi_-^{\frac{2}{3}} - P\left(3 - 2\zeta_+ \xi_-^{\frac{1}{3}}\right) \right) \times$$
$$\left(\zeta_-^2 P^2 + \xi_-^{\frac{2}{3}} - P\left(3 - \zeta_- \xi_-^{\frac{1}{3}}\right) \right) \times \left(-54 P \xi_+ \right)^{-1} \tag{17}$$

with

$$\zeta_+ = 2\phi_r - \varsigma\phi_o \,, \tag{18}$$

$$\zeta_- = -2\phi_r + \varsigma\phi_o \,, \tag{19}$$

$$\xi_+ = \left(\zeta_+ P - 9P\psi - \sqrt{27\Psi} \right)^3 \,, \tag{20}$$

$$\xi_- = -\left(\zeta_+ P + 9P\psi + \sqrt{27\Psi} \right)^3 \,, \tag{21}$$

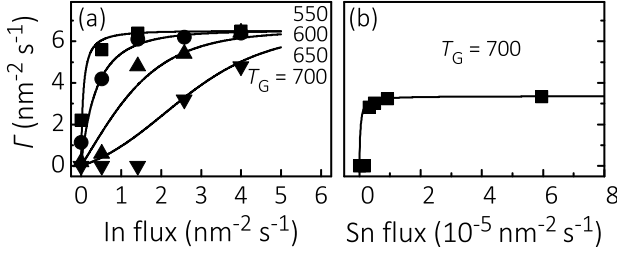$$\psi = \phi_r + \varsigma\phi_o \,, \tag{22}$$

FIG. 5. (a) Growth rate (Γ) of Ga_2O_3 as a function of the In flux at different growth temperatures T_G and an active atomic oxygen flux ϕ_o= 19.2 nm^{-2} s^{-1}. Data are taken from Ref. [5]. (b) Γ of Ga_2O_3 as a function of the Sn flux, with ϕ_o = 7.5 nm^{-2} s^{-1} used for the model. Data are taken from Ref. [22]. Model predictions by Eqs. (10)–(16) are drawn as solid lines using the kinetic parameters given in Table III. The unit of the T_G values given is °C.

and

$$\Psi = P^3 \left(1 + \zeta_-^3 P^2 \varsigma \phi_o + \right.$$
$$\left. + P \times \left(-\phi_r{}^2 + 10\varsigma \phi_r \phi_o + 2\varsigma^2 \phi_o{}^2 \right) \right). \tag{23}$$

The growth rates of Ga_2O_3 and In_2O_3 as presented in Fig. 1 are explicitly modeled with Eqs. (17)–(23).

B. Detailed model of the growth IV-VI materials by S-MBE

The analytical solution for Γ of Eqs. (2)–(4) for IV-VI compound materials is:

$$\Gamma = \frac{1 + P\psi_+ - \sqrt{1 + 2P\psi_+ + P^2\psi_-^2}}{2P} \tag{24}$$

with

$$\psi_\pm = \phi_r \pm \varsigma \phi_o . \tag{25}$$

We predict that Γ of IV-VI materials (e.g., SnO_2)—obtained by S-MBE—may be modeled by Eqs. (24) and (25) with the same accuracy as Γ modeled for III-VI materials (e.g., Ga_2O_3 and In_2O_3) by Eqs. (17)–(23); this is demonstrated in the main text.

C. Conversion factors for ϕ_r and ϕ_o

The model uses reactant fluxes, ϕ_r (e.g., Ga_2O, In_2O, SnO, Ga, In, Sn), and active atomic oxygen fluxes, ϕ_o (from active O_3 or O species), in nm^{-2} s^{-1}.

	Δ_0 (eV)	δ (meV nm^2 s)
Ga_2O_3:In	2.42 ± 0.05 [46]	41 ± 2
Ga_2O_3:Sn	2.91 ± 0.07 [34]	10 ± 2

TABLE III. Values of Δ_0 and δ used in Eq. (14) (main text) for the catalytic model when using In and Sn as catalysts.

The conversion factors for S-MBE used in an ozone MBE system are:

$$\phi_{Ga_2O}^{QCM} = 1\,\text{Å s}^{-1} \rightarrow \phi_{Ga_2O} = 0.38\,\text{nm}^{-2}\,\text{s}^{-1}$$
$$\phi_{In_2O}^{QCM} = 1\,\text{Å s}^{-1} \rightarrow \phi_{In_2O} = 0.25\,\text{nm}^{-2}\,\text{s}^{-1} \tag{26}$$
$$\phi_{SnO}^{QCM} = 1\,\text{Å s}^{-1} \rightarrow \phi_{SnO} = 0.45\,\text{nm}^{-2}\,\text{s}^{-1}$$

$$P_O^{Ga_2O} = 1 \times 10^{-6}\,\text{Torr} \rightarrow \phi_O^{Ga_2O} = 0.73\,\text{nm}^{-2}\,\text{s}^{-1}$$
$$P_O^{In_2O} = 1 \times 10^{-6}\,\text{Torr} \rightarrow \phi_O^{In_2O} = 2.05\,\text{nm}^{-2}\,\text{s}^{-1} \tag{27}$$
$$P_O^{SnO} = 1 \times 10^{-6}\,\text{Torr} \rightarrow \phi_O^{SnO} = 2.25\,\text{nm}^{-2}\,\text{s}^{-1}$$

The reactant fluxes, ϕ_r^{QCM}, are measured prior to growth by a quartz crystal microbalance (QCM) in Å s^{-1}, with the density of the QCM set to 1 g cm^{-3}. These QCM readings are readily converted to absolute fluxes using the known masses of the Ga_2O, In_2O, and SnO molecules that condense onto the QCM. The active atomic oxygen fluxes given result from an oxidant, P_O^r, with mixtures of O_2 and $\sim 10\%$ O_3 in the oxygen molecular-beam [38]. The different oxidation efficiencies were taken from Ref. [17] while using the results obtained for S-MBE.

The conversion factors for conventional MBE used in an oxygen plasma-assisted MBE system are:

$$P_{Ga}^{BEP} = 1 \times 10^{-7}\,\text{Torr} \rightarrow \phi_{Ga} = 1.2\,\text{nm}^{-2}\,\text{s}^{-1}$$
$$P_{In}^{BEP} = 1 \times 10^{-7}\,\text{Torr} \rightarrow \phi_{In} = 0.6\,\text{nm}^{-2}\,\text{s}^{-1} \tag{28}$$
$$P_{Sn}^{BEP} = 1 \times 10^{-7}\,\text{Torr} \rightarrow \phi_{Sn} = 1.5\,\text{nm}^{-2}\,\text{s}^{-1}$$

$$\phi_O^{Ga} = 1\,\text{SCCM} \rightarrow \phi_O^{Ga} = 9.8\,\text{nm}^{-2}\,\text{s}^{-1}$$
$$\phi_O^{In} = 1\,\text{SCCM} \rightarrow \phi_O^{In} = 27.4\,\text{nm}^{-2}\,\text{s}^{-1} \tag{29}$$
$$\phi_O^{Sn} = 1\,\text{SCCM} \rightarrow \phi_O^{Sn} = 30.1\,\text{nm}^{-2}\,\text{s}^{-1}$$

The beam-equivalent pressure (BEP), P_r^{BEP}, of the reactant fluxes is measured prior to growth by an ion gauge in 10^{-7} Torr. P_r^{BEP} is converted from a pressure into a flux using the kinetic theory of gases [47]. The oxygen flux, ϕ_O^r, was

measured in standard cubic centimeters per minute (SCCM), and a radio-frequency plasma power of 300 W was applied. The conversion factors were taken from Ref. [17] and applied to the data given in Ref. [22]. We note the conversion factors [17] and data [22] were obtained in different MBE systems. Thus, the actual conversion may differ slightly due to the different geometries of the MBE systems used. Nevertheless, using the same conversion factors for different MBE systems is a practical and reasonable approach.

IV. ACKNOWLEDGMENTS

* Electronic mail: pv269@cornell.edu

† Electronic mail: schlom@cornell.edu

[1] J. R. Arthur, "*Interaction of Ga and As$_2$ Molecular Beams with GaAs Surfaces*," J. Appl. Phys. **39**, 4032 (1968).

[2] M. Copel, M. C. Reuter, E. Kaxiras, and R. M. Tromp, "*Surfactants in epitaxial growth*," Phys. Rev. Lett. **63**, 632 (1989).

[3] J. Neugebauer, T. K. Zywietz, M. Scheffler, J. E. Northrup, H. Chen, and R. M. Feenstra, "*Adatom Kinetics On and Below the Surface: The Existence of a New Diffusion Channel*," Phys. Rev. Lett. **90**, 056101 (2003).

[4] R. B. Lewis, P. Corfdir, H. Li, J. Herranz, C. Pfüller, O. Brandt, and L. Geelhaar, "*Quantum Dot Self-Assembly Driven by a Surfactant-Induced Morphological Instability*," Phys. Rev. Lett. **119**, 086101 (2017).

[5] P. Vogt, O. Brandt, H. Riechert, J. Lähnemann, and O. Bierwagen, "*Metal-Exchange Catalysis in the Growth of Sesquioxides: Towards Heterostructures of Transparent Oxide Semiconductors*," Phys. Rev. Lett. **119**, 196001 (2017).

[6] K. Ploog, "*Molecular Beam Epitaxy of III-V Compounds: Application of MBE-Grown Films*," Ann. Rev. Mater. Sci. **12**, 123 (1982).

[7] E. Calleja, M. A. Sánchez-García, F. J. Sánchez, F. Calle, F. B. Naranjo, E. Muñoz, S. I. Molina, A. M. Sánchez, F. J. Pacheco, and R. García, "*Growth of III-nitrides on Si(1 1 1) by molecular beam epitaxy Doping, optical, and electrical properties*," J. Crys. Growth **201**, 296 (1999).

[8] S. Fernández-Garrido, G. Koblmüller, E. Calleja, and J. S. Speck, "*In situ GaN decomposition analysis by quadrupole mass spectrometry and reflection high-energy electron diffraction*," J. Appl. Phys. **104**, 1 (2008).

[9] Ziqiang Zhu, Minoru Hagino, Katsuhiro Uesugi, Satomi Kamiyama, Masami Fujimoto, and Takafumi Yao, "*Surface Processes in ALE and MBE Growth of ZnSe: Correlation of RHEED Intensity Variation with Surface Coverage*," Jpn. J. Appl. Phys. **28**, 1659 (1989).

[10] K. Kato, M. Sano, K. Miyamoto, and T. Yao, "*Effect of O/Zn Flux Ratio on Crystalline Quality of ZnO Films Grown by Plasma-Assisted Molecular Beam Epitaxy*," Jpn. J. Appl. Phys. **42**, 2241 (2003).

[11] Akira Hirako, Kazuhide Kusakabe, and Kazuhiro Ohkawa, "*Modeling of Reaction Pathways of GaN Growth by Metalorganic Vapor-Phase Epitaxy Using TMGa/NH$_3$/H$_2$ System: A Computational Fluid Dynamics Simulation Study*," Jpn. J. Appl. Phys. **44**, 874 (2005).

[12] M.-Y. Tsai, O. Bierwagen, M. E. White, and J. S. Speck, "*β-Ga$_2$O$_3$ growth by plasma-assisted molecular beam epitaxy*," J. Vac. Sci. Technol. A **28**, 354 (2010).

[13] P. Vogt and O. Bierwagen, "*The competing oxide and suboxide formation in metal-oxide molecular beam epitaxy*," Appl. Phys. Lett. **106**, 081910 (2015).

[14] P. Vogt and O. Bierwagen, "*Reaction kinetics and growth window for plasma-assisted molecular beam epitaxy of Ga$_2$O$_2$: Incorporation of Ga vs. Ga$_2$O desorption*," Appl. Phys. Lett. **108**, 072101 (2016).

[15] P. Vogt and O. Bierwagen, "*Comparison of the growth kinetics of In$_2$O$_3$ and Ga$_2$O$_3$ and their suboxide desorption during plasma-assisted molecular beam epitaxy*,"

Appl. Phys. Lett. **109**, 062103 (2016).

[16] P. Vogt and O. Bierwagen, "*Kinetics versus thermodynamics of the metal incorporation in molecular beam epitaxy of $(In_xGa_{1-x})_2O_3$,*" APL Mater. **4**, 086112 (2016).

[17] P. Vogt, *Growth Kinetics, Thermodynamics, and Phase Formation of group-III and IV oxides during Molecular Beam Epitaxy*, Ph.D. thesis, Humboldt University of Berlin (2017).

[18] P. Vogt, A. Mauze, F. Wu, B. Bonef, and J. S. Speck, "*Metal-oxide catalyzed epitaxy (MOCATAXY): the example of the O plasma-assisted molecular beam epitaxy of β-$(Al_xGa_{1-x})_2O_3$/β-Ga_2O_3 heterostructures,*" Appl. Phys. Express **11**, 115503 (2018).

[19] M. E. White, M.-Y. Tsai, F. Wu, and J. S. Speck, "*Plasma-assisted molecular beam epitaxy and characterization of $SnO_2(101)$ on r-plane sapphire,*" J. Vac. Sci. Technol., A **26**, 1300 (2008).

[20] Y. Oshima, E. Ahmadi, S. Kaun, F. Wu, and J. S. Speck, "*Sn doping of (010) β-Ga_2O_3 films grown by plasma-assisted molecular beam epitaxy,*" Semicon. Sci.Technol. **33**, 015013 (2018).

[21] Patrick Vogt, Felix V E Hensling, Kathy Azizie, Celesta S Chang, David Turner, Jisung Park, Jonathan P McCandless, Hanjong Paik, Brandon J Bocklund, Georg Hoffman, Oliver Bierwagen, Depdeep Jena, Huili G Xing, Shin Mou, David A Muller, Shun-Li Shang, Zi-Kui Liu, and Darrell G Schlom, "*Adsorption-controlled growth of Ga_2O_3 by suboxide molecular-beam epitaxy,*" APL Mater. **9**, 031101 (2021).

[22] M. Kracht, A. Karg, J. Schörmann, M. Weinhold, D. Zink, F. Michel, M. Rohnke, M. Schowalter, B. Gerken, A. Rosenauer, P. J. Klar, J. Janek, and M. Eickhoff, "*Tin-Assisted Synthesis of β-Ga_2O_3 by Molecular Beam Epitaxy,*" Phys. Rev. Applied **8**, 054002 (2017).

[23] P. Mazzolini, P. Vogt, R. Schewski, C. Wouters, M. Albrecht, and O. Bierwagen, "*Faceting and metal-exchange catalysis in (010) β-Ga_2O_3 thin films homoepitaxially grown by plasma-assisted molecular beam epitaxy,*" APL Mater. **7**, 022511 (2019).

[24] Akhil Mauze, Yuewei Zhang, Takeki Itoh, Feng Wu, and James S. Speck, "*Metal oxide catalyzed epitaxy (MOCATAXY) of β-Ga_2O_3 films in various orientations grown by plasma-assisted molecular beam epitaxy,*" APL Mater. **8**, 021104 (2020).

[25] A. Mauze, Y. Zhang, T. Itoh, E. Ahmadi, and J. S. Speck, "*Sn doping of (010) β-Ga_2O_3 films grown by plasma-assisted molecular beam epitaxy,*" Appl. Phys. Lett. **117**, 222102 (2020).

[26] M. Kneiß, A. Hassa, D. Splith, C. Sturm, H. Von Wenckstern, T. Schultz, N. Koch, M. Lorenz, and M. Grundmann, "*Tin-assisted heteroepitaxial PLD-growth of κ-Ga_2O_3 thin films with high crystalline quality,*" APL Mater. **7**, 022516 (2019).

[27] Mengen Wang, Sai Mu, and Chris G. Van De Walle, "*Role of Ga and In adatoms in the epitaxial growth of β-Ga_2O_3,*" Phys. Rev. B **102**, 035303 (2020).

[28] Kohei S., A. Kuramata, T. Masui, E. G. Víllora, K. Shimamura, and S. Yamakoshi, "*Device-Quality β-Ga_2O_3 Epitaxial Films Fabricated by Ozone Molecular Beam Epitaxy,*" Appl. Phys. Express **5**, 035502 (2012).

[29] P. Mazzolini, A. Falkenstein, C. Wouters, R. Schewski, T. Markurt, Z. Galazka, M. Martin, M. Albrecht, and O. Bierwagen, "*Substrate-orientation dependence of β-Ga_2O_3 (100), (010), (001), and ($\bar{2}01$) homoepitaxy by indium-mediated metal-exchange catalyzed molecular beam epitaxy (MEXCAT-MBE),*" APL Mater. **8**, 011107 (2020).

[30] P. Kisliuk, "*The sticking probabilities of gases chemisorbed on the surfaces of solids,*" J. Phys. Chem. Solids **3**, 95 (1957).

[31] Stephen J. Lombardo and Alexis T. Bell, "*A review of theoretical models of adsorption, diffusion, desorption, and reaction of gases on metal surfaces,*" Surf. Sci. Rep **13**, 1 (1991).

[32] M. A. Lipponer, N. Armbrust, M. Dürr, and U. Höfer, "*Adsorption dynamics of ethylene on Si(001),*" J. Chem. Phys. **136**, 144703 (2012).

[33] P. Vogt and O. Bierwagen, "*Quantitative subcompound-mediated reaction model for the molecular beam epitaxy of III-VI and IV-VI thin films: Applied to Ga_2O_3, In_2O_3, and SnO_2,*" Phys. Rev. Mater. **2**, 120401(R) (2018).

[34] R. Colin, J. Drowart, and G. Verhaegen, "*Mass-spectrometric study of the vaporization of tin oxides. Dissociation energy of SnO,*" Trans. Faraday Soc. **61**, 1364 (1965).

[35] J. Valderrama-N and K.T. Jacob, "*Vapor pressure and dissociation energy of (In_2O),*" Thermochim. Acta **21**, 215 (1977).

[36] K. M. Adkison, S.-L. Shang, B. J. Bocklund, D. Klimm, D. G. Schlom, and Z.-K. Liu, "*Suitability of binary oxides for molecular-beam epitaxy source materials: A comprehensive thermodynamic analysis,*" APL Mater. **8**, 081110 (2020).

[37] *EAG Laboratories* (Syracuse, New York, USA, 2020).

[38] C. D. Theis and D. G. Schlom, (High Temperature Materials Chemistry IX, edited by K.E. Spear, Vol. 97–39, Electrochemical Society, Pennington, 1997) pp. 610–616.

[39] M. Wagner, P. Lackner, S. Seiler, S. Gerhold, J. Osiecki, K. Schulte, L. A. Boatner, M. Schmid, B. Meyer, and U. Diebold, "*Well-Ordered In Adatoms at the $In_2O_3(111)$ Surface Created by Fe Deposition,*" Phys. Rev. Lett. **117**, 206101 (2016).

[40] J. Wintterlin, S. Völkening, T. V.W. Janssens, T. Zambelli, and G. Ertl, "*Atomic and Macroscopic Reaction Rates of a Surface-Catalyzed Reaction,*" Science **278**, 1931 (1997).

[41] D. D. Eley and E. K. Rideal, "*Parahydrogen Conversion on Tungsten,*" Nature **146**, 401 (1940).

[42] L. He, Y. T. Moon, J. Xie, M. Muñoz, D. Johnstone, and H. Morkoç, "*Gallium desorption kinetics on (0001) GaN surface during the growth of GaN by molecular-beam epitaxy,*"

Appl. Phys. Lett. **88**, 071901 (2006).

[43] B. Fu, Z. Jia, W. Mu, Y. Yin, J. Zhang, and X. Tao, "*A review of β-Ga$_2$O$_3$ single crystal defects, their effects on device performance and their formation mechanism*," J. Semicond. **40**, 011804 (2019).

[44] M. D. McCluskey, "*Point defects in Ga$_2$O$_3$*," J. Appl. Phys. **127**, 101101 (2020).

[45] R. Schewski, M. Baldini, K. Irmscher, A. Fiedler, T. Markurt, B. Neuschutz, T. Remmele, T. Schulz, G. Wagner, Z. Galazka, and M. Albrecht, "*Evolution of planar defects during homoepitaxial growth of β-Ga$_2$O$_3$ layers on (100) substrates—A quantitative model*," J. Appl. Phys. **120**, 225308 (2016).

[46] C. B. Alcock, V. P. Itkin, and M. K. Horrigan, "*Vapour Pressure Equations for the Metallic Elements: 298–2500 K*," Can. Metall. Q. **309**, 23 (1984).

[47] D. G. Schlom and J. S. Harris Jr., (Molecular Beam Epitaxy, Chapter 6, Page 544, edited by R. F. C. Farrow, Noyes Publications, New Jersey, USA, 1995).